Journal of Applied Fluid Mechanics, Vol. 18, No. 11, pp. 2775-2790, 2025.
Available online at www.jafmonline.net, ISSN 1735-3572, EISSN 1735-3645.
https://doi.org/10.47176/jafm.18.11.3479

Optimization of Feeding Shoe Design in Powder Conveying Systems: A CFD–DEM Study on Gas-solid Two–phase Flow Dynamics and Structural Parameter Effects

H. Ge, J. Li, L. Zhang, X. Zhang† and C. Zhao

College of Mechanical and Electronic Engineering, Shandong University of Science and Technology, Qingdao 266590, China

†*Corresponding Author Email: zhangxin@sdust.edu.cn*

ABSTRACT

The feeding shoe, which is a critical component that connects the rotary valve to the conveying pipeline, significantly influences the performance of powder conveying systems. The Computational Fluid Dynamics–Discrete Element Method (CFD-DEM) was employed to investigate particle dynamics within various feeding shoe designs under gas–solid two-phase flow conditions. Through comparative analyses of two-phase flow characteristics and particle trajectories, three feeding shoe configurations, namely, through, horn, and funnel types, were evaluated, along with the effects of varying gas velocities. Key structural parameters, including opening diameter and inclination angle, were systematically examined to assess their effect on particle transport efficiency. Results demonstrated that feeding shoes with a low inclination angle or a small opening diameter exhibited poor particle flow, while those with a large opening diameter tended to induce backflow on the left side. By contrast, through-type feeding shoes with a large inclination angle and equal opening diameter achieved optimal conveying performance, minimizing backflow and enhancing flow efficiency. These findings provide theoretical insights for optimizing feeding shoe designs, improving conveying efficiency, and reducing production costs, offering valuable guidance for advancements in powder conveying technology and fluid mechanics.

Article History

Received March 3, 2025
Revised May 21, 2025
Accepted June 23, 2025
Available online September 3, 2025

Keywords:

Computational fluid dynamics–discrete element method (CFD-DEM)
Gas-solid two-phase flow
Particle dynamics
Pneumatic conveying system
Rotary valve feeding shoe

1. INTRODUCTION

In the field of powder pneumatic conveying, the employment of air as the medium for transporting power has made this method the gold standard, endowed with the attributes of safety in transit, exceptional conveying efficiency, and versatility to navigate a variety of conveying paths. The rotary valve, which is an integral connection between the storage repository and the conduit network, channels powdered particulate matter with precision into the pipeline. The transition zone, which is marked by its variable diameter architecture, between the rotary valve and the conduit, is known as the feeding shoe, assuming a pivotal role within the pneumatic conveying infrastructure. The design integrity of the feeding shoe serves as a determinant of the efficacy and fidelity of the conveying process. Alterations to the feeding shoe's configuration may promptly elicit responses in the stability of powder conveyance, while flow dynamics within the feeding shoe can impose constraints on the system's overall performance. Therefore, conducting a comprehensive investigation into the structural attributes and flow characteristics of the feeding shoe is of paramount importance to enhance the operational excellence of a pneumatic conveying system.

In the field of pneumatic conveying, the medium propels granular materials through the system, engendering a multifaceted interplay between the two. Consequently, the blueprint for such systems must be predicated upon an in-depth exploration of gas–solid two-phase flow dynamics. The complexities of this two-phase flow, which involves gas and particulate matter, can be elucidated through the synergistic application of computational fluid dynamics (CFD) and the discrete element method (DEM). The amalgamation of CFD and DEM, known as CFD–DEM, has emerged as a prevalent numerical simulation technique within the scholarly view of pneumatic conveying research. Meanwhile, Zhou et al. (2014)

Nomenclature

c	specific heat capacity	T	temperature
C_z	drag coefficient	u	fluid's velocity vector in the x directions
d_p	equivalent volume diameter of the particles	v	fluid's velocity vector in the y directions
f_x	external force components in the x directions of the fluid	v_g	velocity of the pneumatic conveyor
f_y	external force components in the directions of the fluid	v_s	velocity of the particles
f_z	external force components in the z directions of the fluid	V_p	volume of the powder particles
F_z	viscous drag force on the particles	w	fluid's velocity vector in the Z directions
g	gravitational acceleration	μ	dynamic viscosity
k	heat transfer coefficient	t	time of movement
p	pressure of the fluid	ρ	density of the fluid
r_s	equivalent radius of the solid particles	ρ_p	density of the powder particles
S_T	viscous dissipation term	ρ_g	air density

summarized the two-phase flow law of shaped coal in narrow crevices. Chu et al. (2016) relied on the method of controlling numerical calculation to reduce the error and solve the problems of high cost and large calculation of the two-phase coupling method. Wu et al. (2024) used the CFD–DEM method to explore the regional distribution of material particle swarm collision energy, collision frequency, and collision energy spectrum, providing a theoretical basis for the efficient energy-saving design of a crusher. Bu et al. (2024) used the CFD–DEM model to numerically simulate a Paravisc impeller used for low Reynolds number solid–liquid mixing and improved its structure through its multiphase mixing process (Bu et al., 2024). CFD–DEM stands out for its impressive predictive capabilities, adeptly capturing the intricacies of gas–solid two-phase flow and the trajectory of nonspherical particles with remarkable accuracy. This hybrid approach, which has been recognized for its versatility and precision, has been accepted by numerous researchers, who have successfully applied it to simulate the complex dynamics of gas–solid flows in a multitude of engineering contexts.

Over the past few years, a surge of interest has been observed in the dynamic features of gas–solid two-phase flow, heat and mass transfer laws, and interaction mechanisms among researchers. These scholars have delved into the details of transport phenomena under various conditions, advancing our comprehension of these complex systems and their behavior. Saleh studied parameters related to powder friction charging during thin-phase pneumatic conveying (Saleh et al., 2011). Guo et al. (2013) proposed two prediction models for predicting the pressure drop of the horizontal dense-phase pneumatic conveying of pulverized coal. The structure shows that both models are suitable for the scale of dense-phase pneumatic conveying of pulverized coal at high pressure. Schadauer et al. (2020) studied the effect of air relative humidity on the fluidity of casting powder. Zhao et al. (2020) experimentally investigated the effect of particle initial charge on the minimum picking velocity of pneumatic conveying. Sharma and Mallick (2019) studied the pressure drop of the elbow in pneumatic conveying systems and provided a new bending loss model. Zhou et al. (2023) studied the solid friction coefficient in the horizontal pipe of pneumatic conveying and found that the solid friction coefficient gradually decreased with an increase in the number of air intakes, but increased with an increase in the solid–gas load ratio. Saluja et al. (2024) predicted the pneumatic transportability and fluidity of fly ash by using bulk characterization and found that the angle of repose was the most important parameter of connection transportability and fluidity. Hou et al. (2023) developed a pneumatic micro-feeder for solid pharmaceutical materials, and studies showed that this system can provide a consistent powder flow rate with good repeatability and stability. Hou et al. (2023) used experimental methods to study erosion amount at different positions of bent pipes to determine the maximum erosion position and compared the erosion behavior and mode of single-phase and multiphase flows on bent pipes (Hou et al., 2023). Particle concentration is the major factor that affects the erosion rate of the conveying pipe wall, and the specific erosion rate will decrease under high particle concentration. Macchini et al. (2013) studied the influence of particle concentration on the surface erosion of bent pipes, and experiments confirmed the shielding effect of high particle concentration. Santo et al. (2018a, b) captured the particle velocity and distribution diagram in a dense-phase pneumatic conveying system and found that particle velocity increased linearly with gas velocity, changing the particle mass flow rate, while cross-section gas velocity exerted minimal effect on particle velocity. Increasing conveying gas velocity and particle quantity can extend the length of the particle acceleration section, while increasing pipe diameter will shorten the length of the particle acceleration section. Wang et al. (2025) used a two-fluid model to simulate the hydrodynamic characteristics of a two-stage fluidized bed with an integrated overflow tube. In 2023, Zhang et al. (2023) experimentally investigated the effect of operating conditions (conveying wind velocity and solid mass flow rate) on the wear of whole milk powder in a pneumatic conveying system and measured the effect of four mass characteristics on particle breaking (Zhang et al., 2023). Shang et al. (2023) studied the flow field characteristics of bulk grain pipelines based on gas-solid heterogeneous

coupling, and found that the best conveying effect was achieved when the angle between the filling pipe and the main pipe was 30 degrees. Sun et al. (2023) studied the additional pressure loss coefficient of shotcrete wet mix pneumatic conveying based on CFD-DEM method, and found that the solid-gas ratio and wet mix of shotcrete have a significant impact on pipeline pressure loss.

Scholars have conducted in-depth research on rotary valves, covering all aspects that range from design principles to practical applications. Gundogdu (2004) improved the design of a traditional rotary valve feeder, allowing it to be more flexible for different mass rates of particles. Lourenco et al. (2019) evaluated the effects of average wind velocity and valve velocity on powder and particle feed efficiency. Pezo et al. (2021) studied the effect of a rotary valve feeder with eight blades on the delivery of bulk materials, such as wheat, corn, and rice. Wypych et al. (2006) conducted experimental studies on the feed rate capabilities of rotary valves and blow tank feeders. Yao et al. (2006) performed a study on particle wear in rotary valves, including wear size and shape. Woodruff et al. (2012) designed a new feeder that was specifically for transporting dispersed small particles at a steady gas velocity. Gomes et al. (2021) studied the biomass feeding process in a positive pressure pneumatic conveying system and analyzed the efficiency of the rotary valve and the solid mass flow rate. To enhance the rotary valve's operational excellence, researchers have focused on fine-tuning its performance metrics, escalating efficiency, and diminishing energy requirements. The objective is not only to amplify the valve's utility across a spectrum of industries, including the chemical, culinary, and pharmaceutical fields, but also to propel the rotary valve sector toward innovative and progressive horizons. Dong et al. (2025) used a CFD-DEM coupling model to optimize the new feeder to simulate its process, and found that the response surface method was used to optimize the key structural parameters and significantly improve the stability and uniformity of the feeding fertilizer. Shang et al. (2024) used the gas-solid coupling method to study the flow field characteristics of the flow field of the bulk grain cyclone, and found the optimal structure by measuring the airflow velocity and the bending angle of the main pipe.

Comprehensive analysis shows that most scholars focus on the gas-solid flow characteristics of straight/elbow pipes and the optimization of the performance of the rotary valve body, but the influence mechanism of the variable diameter structure of the feeding shoe on the conveying performance as the "throat" of the system has not been revealed by the system. Traditional studies ignore the coupling relationship between the geometric parameters (opening, inclination) of the feeding shoe and the dynamic behavior of particles, resulting in a lack of theoretical guidance for engineering problems such as clogging and reflow. Although the CFD-DEM method has been widely used in the simulation of gas-solid two-phase flow, there is still a gap in the comparative study of particle escape rate, flow uniformity and conveying characteristics of different feed shoe configurations under multiple gas velocity conditions, which restricts the optimal design of feed shoes.

To address this gap, this research investigated the performance and stability of the rotary valve feeding shoe from an engineering perspective. A coupled CFD–DEM simulation model of the feeding shoe was constructed to simulate particle dynamics. The study compared the conveyance outcomes of three distinct feeding shoe designs, namely, through, funnel, and horn, across various gas conveyance velocities. It involved examining the complex dynamics of two-phase flow within the rotary valve's feeding shoe and tracking the trajectory of powder particles. Particular attention was given to the tapering segment that connects the shoe and the pipe, focusing on the influences of opening diameter and inclination angle. By analyzing these structural parameters, the current study identified strategies for enhancing conveyance performance through optimized design. The findings provide a deeper understanding of the intricate behavior of gas–solid two-phase flow and offer valuable insights for optimizing pneumatic conveying system design, ultimately improving the efficiency of granular material transport.

2. THEORY AND METHODS

2.1 Geometric Model of the Rotary Valve's Feeding Shoe

The pneumatic conveying system, a sophisticated assembly of components including an air compressor, rotary valve, transport pipeline, storage bin, and control system, plays a pivotal role in material transport. The rotary valve, acting as a critical nexus between the storage tank and the conveying line, adeptly facilitates the transfer of powder into the pipe-line. The transitional region between the rotary valve and the pipeline, characterized by a variable diameter, is designated as the feeding shoe. This element, integral to the pneumatic conveying system, significantly influences the efficiency and stability of powder conveyance. The structural diversity of the feeding shoe manifests in the varying transitions of diameter between the rotary valve and the pipeline.

These transitions delineate three distinct categories of feeding shoes: through, horn, and funnel types, each distinguished by the diameter of diameter reduction. The aperture extent and incline angle serve as influential factors that directly determine the diameter reduction within the feeding shoe. Through precise manipulation of these variables, the feeding shoe guarantees a seamless flow of granular material, fore-stalling obstructions and backflow under the influence of airflow. The upper particle inlet opening diameter W, lower particle opening diameter N, and feeding shoe incline angle β emerge as salient features. By adjusting these distinct variables, the classification of material shoes can be further refined. Following the specific parameters of the storage tank and pipeline, the N and β can be modified without altering the upper inlet opening diameter W, Table 1 lists the model parameters. This strategic com-bination of variables facilitates the construction of a corresponding model, as detailed in the illustrative Fig. 1, thereby optimizing the functionality of the feeding shoe with-in the pneumatic conveying system.

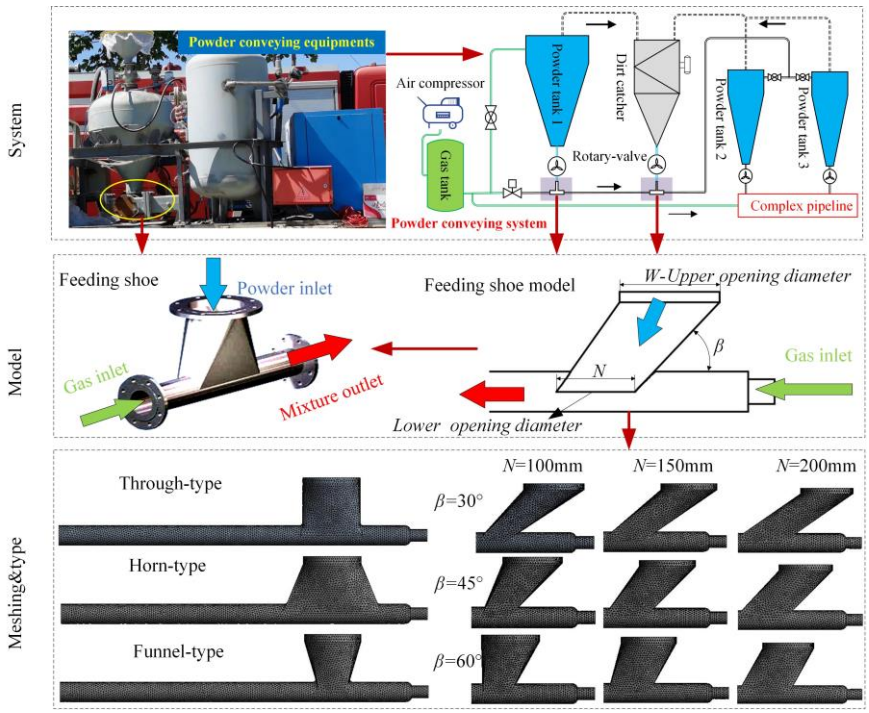

Fig. 1 Model of feeding shoe

Table 1 Model parameter settings

Model parameter	value
Feed shoe type	through, horn, funnel
Upper particle inlet opening *W*	300mm fixed
Lower particle opening *N* (mm)	100,150,200,250,300
Feed shoe inclination β	30°, 45°, 60°

In adherence to the principles of preserving essential characteristics and enhancing computational efficiency, the model undergoes a transformation, guided by the criterion of similarity. The geometric configuration of the system is proportionally reduced to 1:20 scale, ensuring comprehensive hydrodynamic similarity (geometric, kinematic, and dynamic) between the scaled model and prototype. This scaling methodology guarantees that all governing fluid parameters exhibit deterministic scaling relationships at homologous spatial-temporal positions within the flow field. This meticulous scaling process enables a more streamlined analysis, preserving the fidelity of the original phenomenon while reducing computational demands, as detailed in the illustrative diagram (Zhang et al., 2024).

The feeding shoe model, meticulously scaled to reflect its actual dimensions, has been constructed, with the internal fluid domain delineated accordingly. Utilizing the Meshing Mode within the FLUENT software suite, the model's fluid domain has been partitioned into a network of computational cells. The granularity of this mesh is pivotal, as it profoundly influences the fidelity of the simulation outcomes; suboptimal grid quality may precipitate numerical instability, culminating in the divergence of the computational workflow. The refinement of the mesh directly correlates with the precision of the simulated data; however, this refinement also amplifies the computational load, necessitating enhanced computational resources. Consequently, the selection of an appropriate mesh size is a critical decision, that requires judicious consideration. In the vicinity of the wall, the boundary layer is discretely partitioned using the poly algorithm, and the region is subsequently populated with a tetrahedral mesh, ensuring a balance between computational efficiency and the resolution of near-wall phenomena.

2.2 Theoretical Analysis of Gas and Solid Phase

2.2.1. Turbulence Model

The gas flow in the pipe model is completely turbulent, ignoring the viscosity between the molecules. In the selection of turbulent phases, the Reynolds averaging method has a relatively small amount of calculation, which can simulate most of the turbulent phenomena in the flow field, which is more in line with the actual flow field environment. The turbulence models included in the Reynolds averaging method are: k-ε model, single equation (Spalart-Allmaras) model, and k-ω model. The standard k-ε model is the most widely used typical two-way turbulence model among turbulence models.

$$\mu = \rho C_{\mu} \frac{k^2}{\varepsilon} \tag{1}$$

where μ is the turbulent viscosity, which can be expressed as a function of k and ε; C_{μ} is an empirical constant.

The equation for incompressible turbulent flow energy is:

$$\frac{\partial k}{\partial t} + \overline{u_i} \frac{\partial k}{\partial x_i} = \frac{\partial}{\partial x_i}\left[\left(\nu + C_k \frac{k^2}{\varepsilon}\right)\frac{\partial k}{\partial x_i}\right] + \nu_t \left[\frac{\partial \overline{u_i}}{\partial x_j} + \frac{\partial \overline{u_j}}{\partial x_i}\right]\frac{\partial \overline{u_i}}{\partial x_j} - \varepsilon \tag{2}$$

The turbulence ripple equation is:

$$\frac{\partial \varepsilon}{\partial t}+\overline{u_i}\frac{\partial \varepsilon}{\partial t}=\frac{\partial}{\partial x_i}\left[\left(v+C_\varepsilon\frac{k^2}{\varepsilon}\right)\frac{\partial \varepsilon}{\partial x_i}\right]+c_{1\varepsilon}v_t\left[\frac{\partial \overline{u_i}}{\partial x_j}+\frac{\partial \overline{u_j}}{\partial x_i}\right]\frac{\partial \overline{u_i}}{\partial x_j}-c_{2\varepsilon}\frac{\varepsilon^2}{k} \quad (3)$$

The above equation forms a standard k-ε equation, where C_k, C_ε, $c_{1\varepsilon}$ and $c_{2\varepsilon}$ are empirical constants.

2.2.2 Gas Phase Equation

The basic equations of fluid motion are the basis for solving fluid motion, which follows the equations of conservation of mass, momentum, energy, and thermodynamics. In the calculation process, it is also necessary to consider the swirl, turbulence and other factors according to the actual situation, and add the constraint equation to the basic equation system. The gas-phase dynamics in the coupled system are governed by the N-S equations (Versteeg & Malalasekera, 1995), with its behavior being numerically resolved through the simultaneous solution of the continuity equation and momentum conservation principles.

The gas-phase continuity equation is:

$$\frac{\partial \varepsilon\rho}{\partial t}+\nabla\cdot\rho\varepsilon u=0 \quad (4)$$

where ρ is the density of the fluid; t for time; u is the fluid flow rate; ε is a volume fraction term.

The equation for the conservation of momentum is：

$$\frac{\partial \varepsilon\rho\upsilon}{\partial t}+\nabla\cdot\rho\varepsilon\mu\upsilon=-\nabla\rho+\nabla\cdot\left(\mu\varepsilon\nabla\upsilon\right)+\rho\varepsilon g-S \quad (5)$$

where g is the acceleration due to gravity; μ is sticky; the interphase momentum transfer between gas and particulate phases arises from their velocity differential, with hydrodynamic resistance acting on particles quantified through a momentum exchange term (S). This term, serving as a bidirectional coupling mechanism in Eulerian-Lagrangian frameworks, is mathematically expressed as:

$$S=\frac{\sum_{i=1}^{n}F_D}{v} \quad (6)$$

where v is volume of calculated cell.

2.2.3 Solid Phase Equation

Establish a force equilibrium equation to describe the motion of each individual particle. The trajectory of a particle can be expressed as:

$$\frac{du_p}{dt}=\frac{u_g-u_p}{\tau_p}+\frac{g\left(\rho_p-\rho_g\right)}{\rho_p}+F_p \quad (7)$$

where g is the gravitational constant; Subscript p and g description of the gas phase and solid particles; $\frac{u_g-u_p}{\tau_p}$ represents the gas resistance (drag force), which τ_p is the relaxation time of the particles; $\frac{g\left(\rho_p-\rho_g\right)}{\rho_p}$ represents the buoyancy term, ρ_p which is the density of the powder particles; F_p represents gravity, pressure gradient force, virtual mass force, and Safman lift, among others. The particle relaxation time is calculated as:

$$\tau_p=\frac{\rho_p d_p^2}{18u_G}\frac{24}{C_D\,\mathrm{Re}} \quad (8)$$

considering the spherical particles with uniform diameter (d_p) and small particle size in this study, the Mursi-Alexander drag model for spherical particles was adopted. The drag coefficient (C_D), which depends on the particle Reynolds number (Re), is determined by the following expression:

$$C_D=a_1+\frac{a_2}{\mathrm{Re}}+\frac{a_3}{\mathrm{Re}^2} \quad (9)$$

The model incorporates three empirical constants (a_1, a_2, and a_3) corresponding to different Reynolds number regimes as defined by Mursi and Alexander. The gas-solid relative Reynolds number is computed through the following relationship

$$\mathrm{Re}=\frac{\rho_g d_p\left|u_p-u_g\right|}{u_g} \quad (10)$$

The expressions for gravity, Safman lift, pressure gradient force, virtual mass force are:

$$F_g=mg=\rho_p V_p g \quad (11)$$

$$F_{sa}=m_p\frac{2K\mu_g^{1/2}\rho_g d_{ij}}{\rho_p d_p\left(d_{ij}\cdot d_{ji}\right)^{1/4}}\left(\vec{u}_g-\vec{u}_p\right) \quad (12)$$

$$F_{gp}=m_p\frac{\rho_g}{\rho_p}\vec{u}_g\nabla\vec{u}_g \quad (13)$$

$$F_{am}=0.5m_p\frac{\rho_g}{\rho_p}\left(\vec{u}_p\nabla\vec{u}_p-\frac{d\vec{u}_p}{dt}\right) \quad (14)$$

where V_p is the volume of the powder particles.

2.3 Numerical Simulation Method and Parameter Setting

In pneumatic conveying simulation, FLUENT software is widely used for its turbulence modeling capabilities. However, it is limited to macroscopic particle flow analysis and cannot simulate individual particle forces and movements. This study, focused on powder flow characteristics within pipes, highlights FLUENT's limitations. Powder particle collisions and interactions with the pipe wall, critical in pneumatic conveyance, can be effectively simulated using EDEM software based on the DEM. However, EDEM does not cover fluid dynamics, limiting its standalone use. To overcome these limitations, this study employs a FLUENT-EDEM coupling method to analyze particle flow dynamics within tubes, and the specific coupling process is shown in Fig. 2. Appropriate parameters and interfaces were established for seamless software integration, using the Dynamic Drag-Particle Method (DDPM) interface for data exchange. This approach allows simultaneous consideration of particle forces and interactions within the flow field.

The simulation model includes a velocity inlet and pressure outlet, using a three-dimensional pressure-based

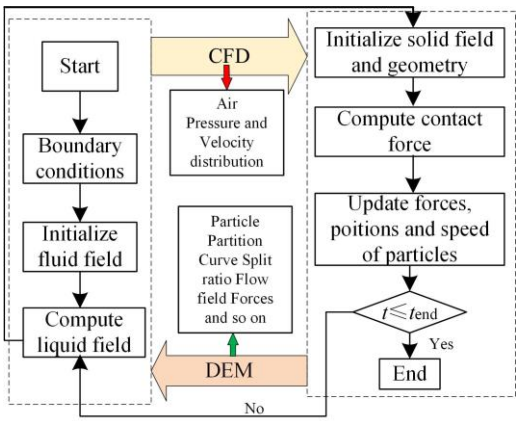

Fig. 2 CFD-DEM coupling process

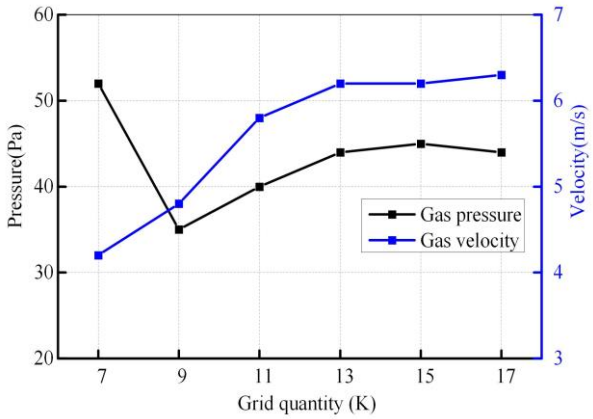

Fig. 3 Results of the grid independence test

Table 2 Simulation Parameters and Settings

Particle parameter	value
Diameter	100μm
Poisson's ratio	0.25
Density	700 kg/m^3
Shear modulus	2.5×10^7 Pa
Solid-gas ratio	10~40
Mass flow rate	1.39 g/s
Time step	1.5×10^{-7} s
Particle-particle coefficient of recovery	0.1
Particle-particle static friction Coefficient	0.7
Particle-particle rolling friction Coefficient	0.01
Gas parameter	value
Particle velocity	1 m/s
Gas velocity	25.56~40.4 m/s
Viscosity	1.78×10^{-5}kg/m·s^{-1}
Density	1.225 kg/m^3
Time step	2×10^{-5} s
Number of time steps	5000
Simulation time	0.1 s
Particle-wall coefficient of recovery	0.3
Particle-wall rolling friction Coefficient	0.02
Particle-wall static friction Coefficient	0.5

solver. A no-slip boundary condition is applied to the tube wall, and the SIMPLE (Semi-Implicit Method for Pressure-Linked Equations) algorithm is used for pressure-velocity coupling. This comprehensive approach provides a nuanced understanding of particle flow dynamics within tubes, the convergence residuals are 10^{-5}. Table 2 shows in detail the initial conditions and boundary parameters for gases and particles in FLUENT and EDEM simulations.

2.4 Numerical Simulation Method and Parameter Setting

The internal fluid domain was isolated and meshed using ANSYS FLUENT (Meshing Mode). A poly mesh was employed for the bulk domain, with boundary layer refinement applied near the walls to resolve viscous effects, while the remaining volume was filled with tetrahedral elements. Although finer meshes yield more precise results, they also demand greater computational resources. To determine the optimal balance, a grid independence study was performed by evaluating six mesh densities: 70k, 90k, 110k, 130k, 150k, and 170k cells. The gas velocity and pressure at the straight-pipe outlet were monitored as key validation parameters. As demonstrated in Fig. 3, both velocity and pressure exhibited negligible variation beyond 130k cells, indicating solution convergence at this resolution. Consequently, the 130k-cell mesh was selected for all subsequent simulations, ensuring computational efficiency without compromising result reliability.

The feed pipe system of the rotary valve comprises interconnected horizontal and vertical sections. While numerous studies have investigated simplified horizontal-vertical piping systems, the current work validates computational accuracy through direct comparison with experimental data from Yan et al., the researchers utilized PIV coupled with sophisticated image analysis methods to quantitatively investigate the hydrodynamic behavior of gas-solid flows in horizontal pipelines. Their experimental approach enabled comprehensive measurement of key flow parameters, including: instantaneous velocity fields, spatial distribution of particulate phase concentration, and axial pressure gradient variations (Yan & Rinoshika, 2012). For experimental validation, a monitoring station was established 0.3 m downstream from the feed shoe outlet. Radial particle concentration profiles were obtained through systematic data processing of experimental measurements. Figure 4 presents the comparative results between simulation and experimental data, revealing that while minor quantitative discrepancies exist, the CFD-DEM simulations successfully reproduce the fundamental trends observed experimentally. This strong agreement in distribution patterns demonstrates both the validity of the numerical model and the robustness of the coupled CFD-DEM methodology.

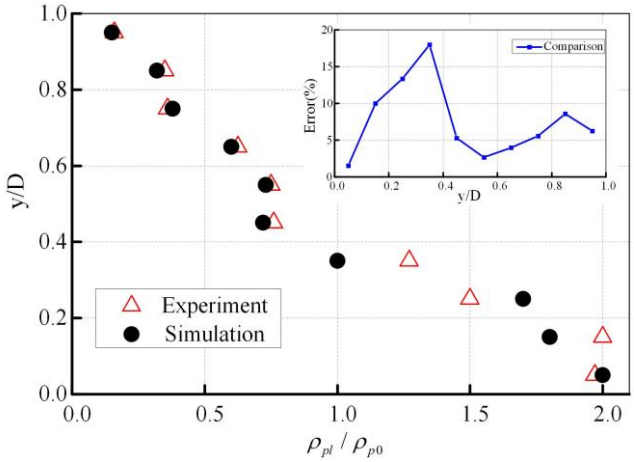

Fig. 4 Model verification test

3. ANALYSIS OF THE CONVEYING PERFORMANCE OF THE ROTARY VALVE'S FEEDING SHOE

3.1 Analysis of Influence of Gas Conveying Velocity on Particle Flow

In the current study, numerical simulations of the flow field within feeding shoes were conducted, with air inlet velocities systematically varied (25.6, 31.3, 36.1, and 40.4 m/s) to elucidate the influences of internal velocity field, pressure field, and particle trajectory on overall performance. By examining the evolution of cloud images, subtle distinctions in the internal flow dynamics of the feeding shoe across different inlet air velocities were discerned, revealing the underlying mechanisms that governed the interaction between the velocity field and the pressure field. Furthermore, meticulous tracking of particle trajectories enabled the precise movement paths of particles within the feeding shoe to be ascertained at varying conveying gas velocities.

Figure 5 presents a detailed visualization of the gas velocity flow patterns across the central section of feeding shoes, with the gas inlet velocity ranging from 25 m/s to 40 m/s. The analysis reveals the presence of eddy currents at the discharge orifices of through- and horn-type feeding shoes. As the velocity of conveying gas increases, these eddy currents progressively expand. Notably, the velocity flow lines of the trumpet-type feeding shoe exhibit a smoother profile compared with those of the through type, with reduced curvature and fewer directional changes in the flow lines. This characteristic is advantageous for the efficient transportation of particles driven by gas flow. Conversely, the internal flow lines within the feeding port of the funnel-type feeding shoe exhibit a more disordered arrangement. Despite the increase in conveying gas velocity, the velocity flow lines undergo minimal alteration. Consequently, a substantial portion of the gas stream linearly traverses the pipeline, experiencing minimal interference from particles. Only a minor fraction of the gas flow infiltrates the apex of the feeding port, suggesting a less uniform gas distribution and potentially affecting the overall performance of particle conveyance in this configuration.

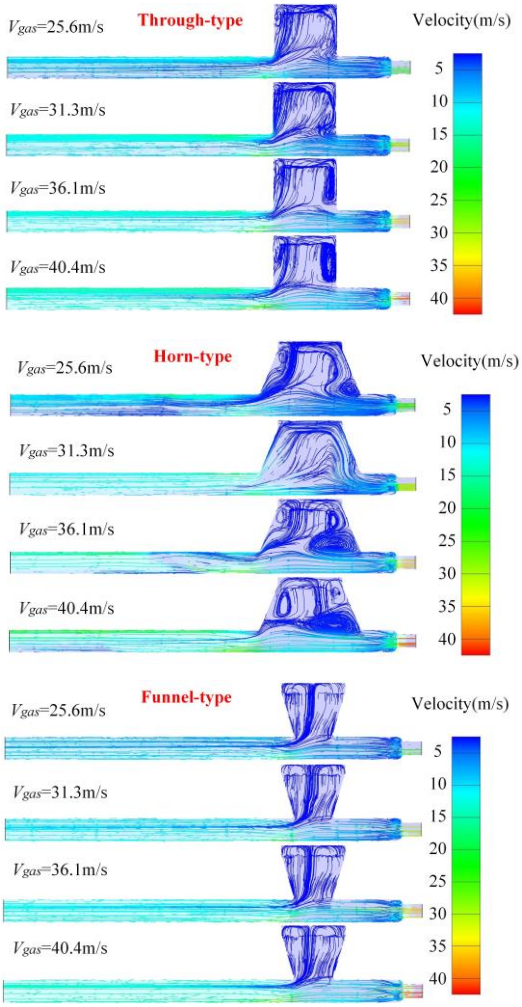

Fig. 5 Velocity flow line of center section at different gas velocities

Figure 6 shows the intricate topography of relative gas pressure distribution within the central section of the conveying pipeline at varying gas velocities for through, horn, and funnel inlets. The investigation reveals that gas pressure in the inlet pipeline consistently surpasses that in the outlet pipeline, with a distinct gradient shift in pressure observed throughout the entire conduit. As conveying gas velocity increases from 25.6 m/s to 40.4 m/s, the maximum pressure of the through type rises from 2071 Pa to 3870 Pa. Similarly, the horn type experiences a rise in maximum pressure from 2650 Pa to 3632 Pa, while the funnel type exhibits an increase from 2142 Pa to 3248 Pa. Notably, the maximum pressure of the horn type remains virtually unchanged at 25.6 m/s and 31.3 m/s. Furthermore, other pressure fluctuations exhibit a discernible stepwise incline as gas velocity increases, indicating a consistent pattern in the pressure dynamics of the system.

To elucidate the effect of conveying gas velocity on pressure and velocity within the inlet port and the conveying pipeline, the inlet port and outlet port cross sections were meticulously selected for data analysis, as shown in Fig. 7. The investigation culminated in a curve diagram that illustrates the average pressure of the two sections as it varies with inlet gas velocity. As inlet

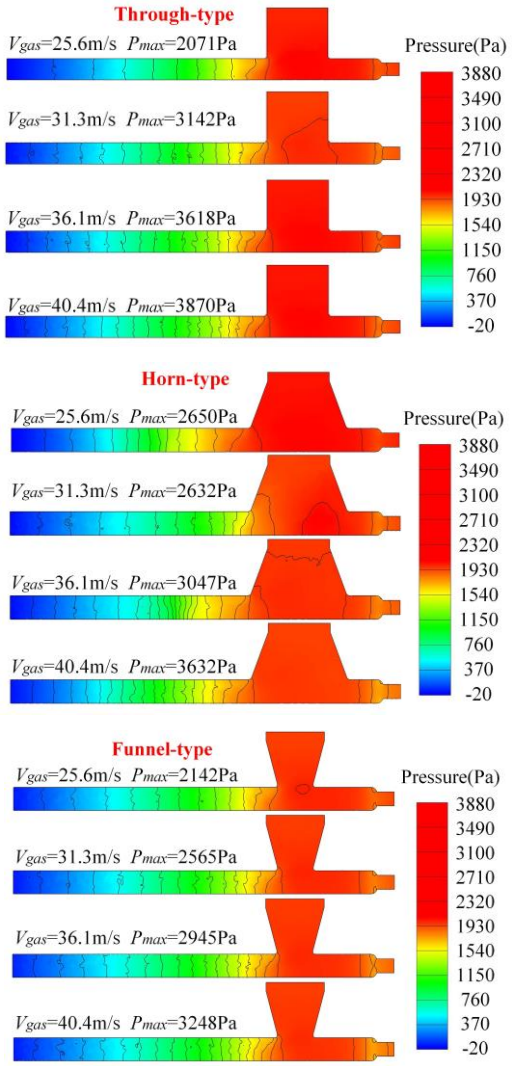

Fig. 6 Pressure diagram of central section at different gas velocities

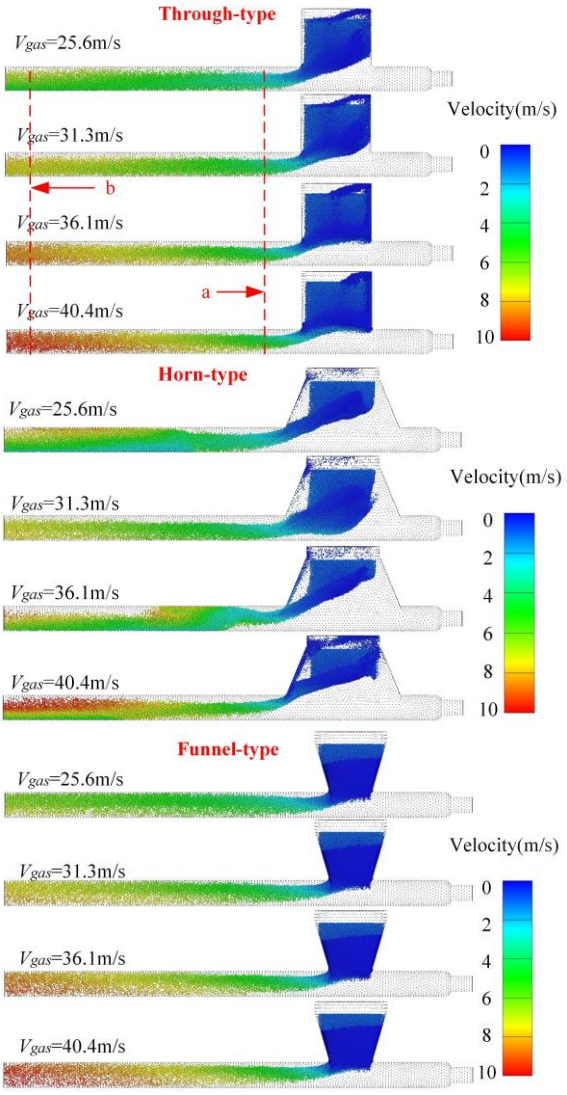

Fig. 8 Particle trajectories at different gas velocities

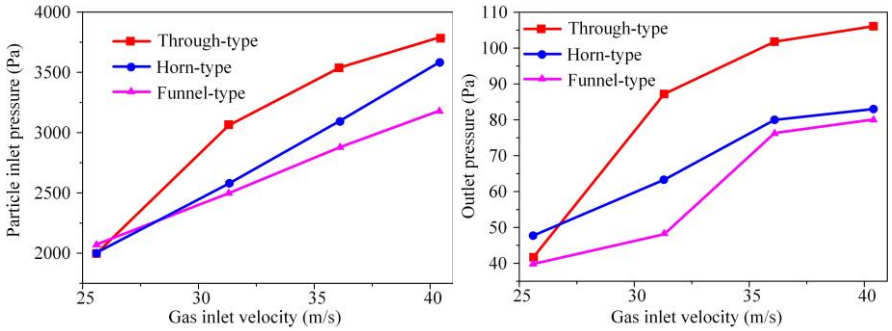

Fig. 7 Variation curve of inlet and outlet pressure of particles

velocity increases, a corresponding rise in average pressure at the inlet and the outlet of the conveying pipe is observed. Within the velocity range of 25 m/s to 40 m/s, the pressure of the through type consistently surpasses those of the horn and funnel types. Moreover, the pressure differential between the particle inlet and outlet is noteworthy, with inlet pressure significantly exceeding outlet pressure. This substantial pressure disparity facilitates the efficient conveying of material particles from import to export, enhancing the transport process.

As depicted in Fig. 8, particles are subjected to the influences of gravitational force and gas flow upon entering the conveying pipeline from the inlet, inducing turbulent phenomena. Following a series of swirling, colliding, and frictional interactions within the inlet section, the particles transition into the conveying

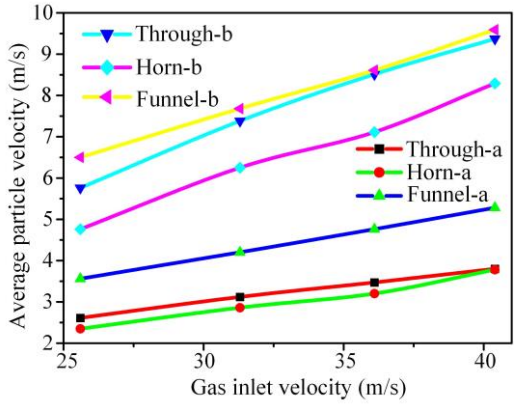

Fig. 9 Particle velocity curve of pipeline section

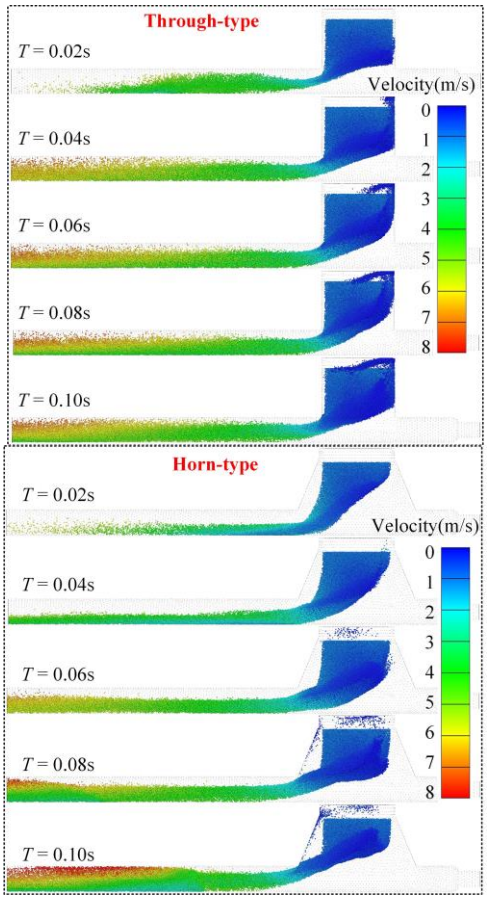

Fig. 10 Particle velocity diagram at different times

pipeline, where they coalesce into a stable conveying flow that is predominantly situated near the middle of the pipeline. The particle velocity distribution within the through-type feeding shoe pipeline exhibits uniformity. Notably, the majority of particles at the through-type feeding port are propelled upward, with a subset continuing to swirl, ultimately contributing to material port accumulation. Particle velocity at the top of the pipe surpasses that at the bottom, accompanied by a modest upward flow of particles. A plug formation is observed when inlet velocity reaches 36.1 m/s. By contrast, the funnel-type feeding shoe, which is characterized by its diminutive size, impedes timely transportation, leading to a gradual accumulation of particles. This accumulation precipitates material inlet powdering, with a reduced presence of particles within the flow pipe. Interestingly, particle velocity at the bottom of the pipeline exceeds that at the top.

To achieve precision in the measurement of particle velocity, the mean particle velocities at positions a and b must be computed individually. At position a, which is located at the inception of the pipe beneath the blanking port, particle velocity direction has recently undergone alteration, resulting in a correspondingly lower velocity. Conversely, position b is situated at the exit of the conveying pipeline, where particles have traversed a substantial distance under the influence of gas, leading to a marked increase in velocity. Examination of the data presented in Fig. 9 reveals that the average particle velocities at positions a and b within the funnel tube exceed those observed in the two other pipeline configurations. This discrepancy can be attributed to the reduced number of particles that enter the tube, which, in turn, diminishes the resistance encountered by gas. Consequently, the cumulative force exerted on each particle is greater compared with that experienced by particles in the through tube and the horn tube, resulting in higher acceleration for particles within the funnel tube. This phenomenon contributes to the elevated mean particle velocity within the funnel tube. In parallel, the horn tube has the highest particle density, which correspondingly impedes the flow and results in the smallest average particle velocity.

The funnel shoe exhibits suboptimal conveying performance and is prone to blockages. Conversely, the through and horn designs demonstrate upward particle trajectories. Figure 10 illustrates the evolution of particle velocity distributions within the through tube and the funnel tube at intervals when conveying gas velocity reaches a steady 25.6 m/s. This analysis delves into the intricate process of particle reflux and bolt formation, revealing concurrent yet distinct patterns. During the initial time frame from T=0.04–0.1 s, particle velocity dynamics in the through shoe's conduit remained largely consistent. However, a stratification phenomenon occurred at different moments, as high-velocity particles ascended to the pipe's upper reaches, suspended in dynamic equilibrium. The analysis revealed a remarkable constancy in particle velocity at the radial cross sections of the pipe, unaffected by the passage of time and retaining a stable profile. At the T=0.04 s mark, particles congregate at the base of the conduit, their velocities exhibiting a uniform hue. By T=0.06 s, a modest acceleration is discernible near the outlet, signaling a subtle shift in particle dynamics. At T=0.08 s, the emergence of velocity stratification near the outlet's proximal end is noted, with particles at the pipe's zenith displaying a red-coded velocity, which is indicative of their superior velocity relative to their counterparts at the base. The stratification phenomenon becomes more pronounced at T=0.10 s, extending to the distal end of the outlet, and a marked increase in particle count within the tube is observed. The analysis reveals that particle velocity undergoes temporal variations at identical radial cross-section positions, manifesting periodic fluctuations. This cyclical behavior underscores the complex interplay of forces that govern particle flow within the system.

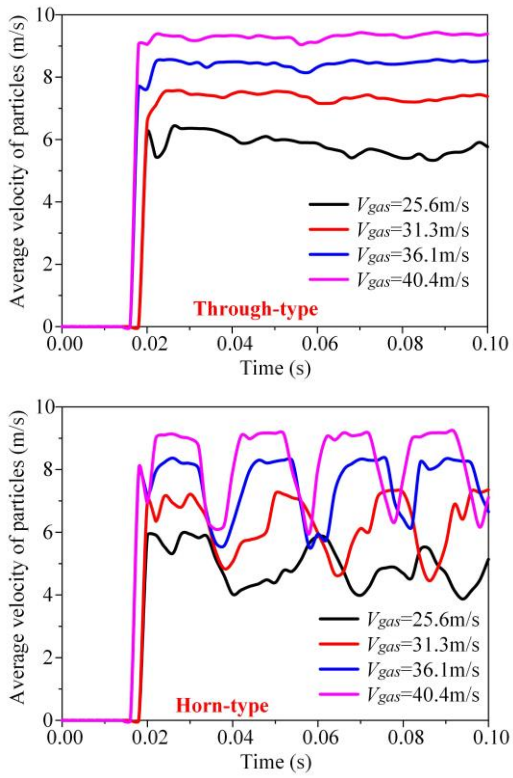

Fig. 11 Average velocity of particles at the outlet

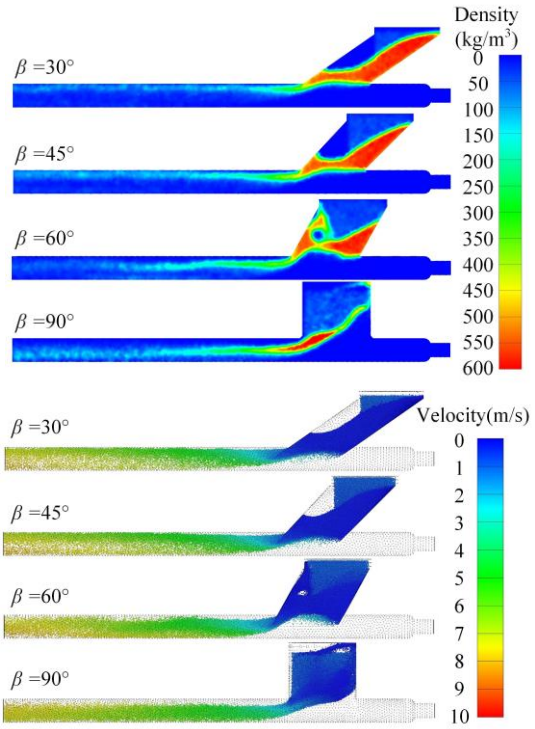

Fig. 12 Particle concentration and trajectory at different inclination angles

To substantiate this hypothesis, the ensemble velocity at fixed exit points was quantitatively assessed, and a temporal velocity profile was mapped with time as the orthogonal axis. On the left of Fig. 11, the evolving particle velocity trajectory within a through-type conduit is presented. As particles traverse T=0.02 s, initial fluctuations are minimal, gradually settling into a steady state. The influence of accelerating carrier gas is manifested in the gradual escalation of average particle velocity. Conversely, the horn-type conduit's outlet dynamics, shown on the right, reveals a distinct pattern. Upon particle egress at T=0.02 s, their velocity oscillates periodically, with an approximate cycle of 0.02 s. Both graphical representations align seamlessly with the proposed hypothesis, validating its empirical foundation.

A comparison of the velocity profiles of the two distinct pipes reveals notable differences in particle dynamics under constant conveying gas velocity. Within the same temporal span, the traversed distance of particles in the through type is conspicuously greater than that in its horn-shaped counterpart, consequently yielding a larger area under the velocity curve for the former. This phenomenon underscores the superiority of the through pipe in transport, exhibiting enhanced efficiency and extended range. The movement of particles within the through pipe exhibits a more fluid and consistent motion, diminishing inter-particle friction and resistance, and consequently augmenting transmission efficiency and precision. Conversely, the horn-shaped pipe, despite its advantages in certain contexts, falls short in overall suitability for long-distance transport. It is less adept at fulfilling the stringent demands of industrial production, particularly in terms of transportation efficiency and stability. In essence, a linear pipe's transmission characteristics foster a more conducive environment for particle movement, making it a favorable choice for large-scale transport applications.

3.2 Analysis of the influence on structural factors of feeding shoes

3.2.1. Effect of Feeding Shoe Incline Angle β on Particle Flow

The analysis of particle conveyance across the three distinct structural configurations of feeding shoes reveals that the through pipe excels in particle transport. Within this framework, altering the incline angle of the feeding shoes and exploring various structural designs are imperative. A comprehensive investigation into the pivotal structural parameters of the feeding shoe and their effects on flow performance has been conducted. The examination of particle concentration and velocity profiles at β=30°, 45°, 60°, and 90°, as depicted in Fig. 12, indicates that particles accumulate to varying extents at the base of the discharge port for β=30°, 45°, and 60° inclinations. With an increase in angle, the area of particle accumulation diminishes. For smaller inclinations, particles continuously descend and adhere to the inner wall of the shoe tube. The influence of particle fluidity is evident, because the influx of particles into the pipeline is significantly lower than the generation rate. Notably, the high-concentration region for β=30° extends toward the apex of the discharge port. Prolonging the simulation duration will result in particles filling the entirety of the shoe, culminating in obstruction. In summary, the through pipe configuration demonstrates superior particle conveyance, necessitating the strategic adjustment of feeding shoe angles and structural modifications to optimize flow performance and mitigate potential blockages.

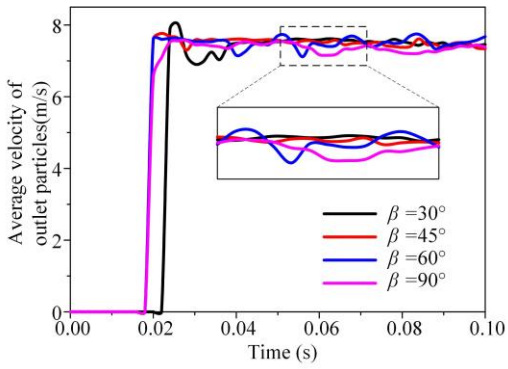

Fig. 13 Particle velocity curves at different angles

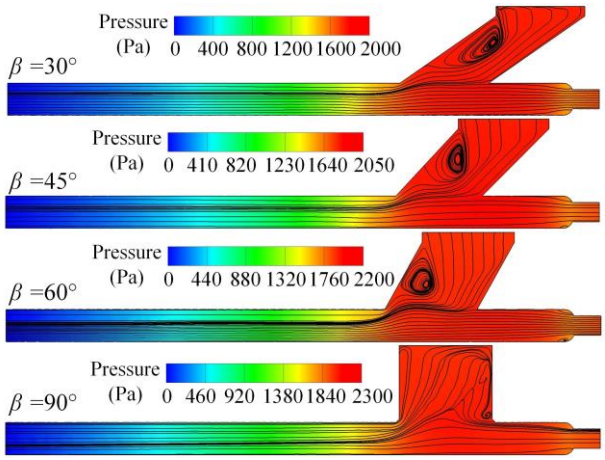

Fig. 14 Pressure diagram of center section at different inclination angles

In the β=60° scenario, a substantial number of particles experienced retrograde reflux on the left side of the shoe, primarily due to their initial downward velocity being vertical. Upon first contact with the right side of the shoe tube wall, solid particles began to accumulate, and density progressively decreased in the direction of gas flow. Consequently, the reduced particle count on the left side made it susceptible to gas influence. By contrast, the β=90° through type exhibited a minimal degree of particle reflux on the right side of the material shoe. This phenomenon can be attributed to the initial direction of particle movement being vertical downward, aligning perfectly with the pipe wall's structure. A slight gap between the descending particles and the right side of the pipe wall facilitated the passage of a small gas volume, which, in turn, drove a minor particle reflux. However, the limited particle quantity exerted a negligible effect on overall transport.

Through a comparative analysis of particle exit velocities, the subtle effect of the inclination angle β on particulate transport can be discerned, as depicted in Fig. 13. The time evolution of the mean particle velocities across the four distinct pipelines with varying inclinations exhibits a steady profile. Notably, the disparity in velocity across different angles remains relatively inconspicuous. Focusing on the temporal interval T=0.05–0.07 s, a discernible trend emerges as follows: average velocity rises as incline diminishes. This velocity variation reflects the underlying particle flux dynamics to a certain extent. In simpler terms, the comparative study of particle velocities displays a nuanced correlation between the inclination angle and the stability of particle transport, with the rate of change in velocity mirroring the quantitative differences in particle count under varying inclinations. The temporal snapshot during T=0.05–0.07 s serves as a telling indicator of this interplay.

To elucidate pressure distribution within the tube, the central section pressures (relative to ambient values) were sampled simultaneously across various inclination angles β. In accordance with Fig. 14, the analysis reveals the formation of eddies on the left side of the feeding shoe at β=30°, 45°, and 60°, with their intensity diminishing progressively. Conversely, at β=90°, the propensity for eddy formation shifts to the right side of the feeding shoe. The gas inlet and the pressure range within the shoe exhibit a consistent profile. Notably, pressure within the tube exhibits a gradual decline from the inlet to the outlet, while peak pressure within the tube escalates along with the increasing inclination angle.

3.2.2. Effect of the Lower Opening Diameter *N* Of the Feeding Shoe on Particle Flow

In the search for diverse shoe structures, the interplay of various angles and opening diameters of feeding shoes offers a myriad of possibilities. By adjusting the opening diameter N in response to β=30°, 45°, and 60°, the distribution and transport efficacy of particles are examined. Figure 15 shows that when β=30°, a particle buildup emerges at the blanking port. As the lower opening diameter is amplified, the particle accumulation issue achieves a slight improvement, but falls short of a definitive resolution, merely postponing the clogging time of the shoe. When β=45°, the area of particle buildup diminishes compared with when β=30°. However, the accumulation problem escalates with increasing lower opening diameter N. However, when N surpasses the upper opening diameter W, a reverse flow of particles becomes evident on the left side of the shoe. When β=60°, the number of particles that are refluxing progressively increases along with the amplification of N.

In summary, a diminutive opening diameter coupled with a reduced inclination angle engenders particle accumulation, culminating in the obstruction of the shoe. Conversely, an increased inclination angle fosters particle conveyance. Increasing the opening diameter ameliorates the issues of particle accumulation and clogging to a certain extent. However, it inadvertently precipitates reflux, which is antithetical to efficient particle transportation. The conveyance efficacy of particles within the shoe and the pipeline is further influenced by the magnitude and orientation of the particles' initial velocity. In alignment with the practical application of a rotary valve feeding shoe, this study posits a vertical downward orientation for the initial velocity direction of particles.

Figure 16 illustrates the comparative curves of particle velocity and outflow quantity for different opening diameters at the pipe exit, with identical particle positions

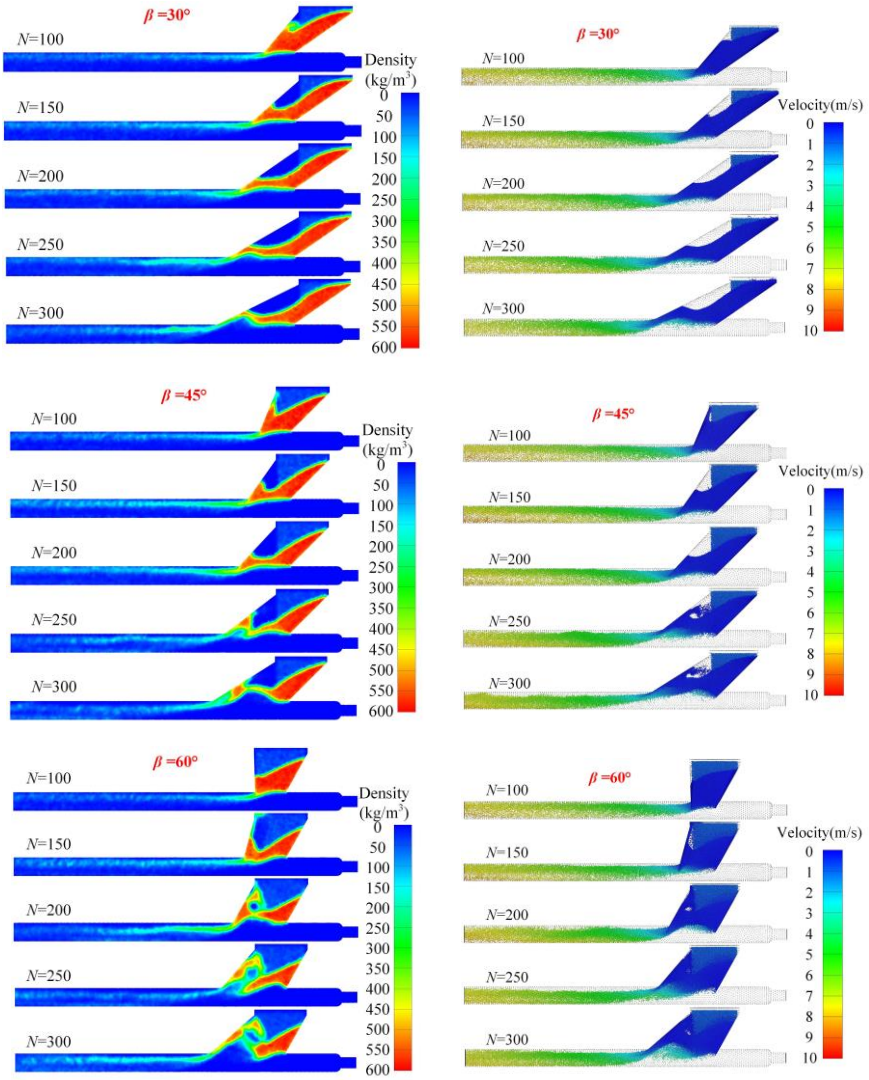

Fig. 15 Particle concentration and trajectory at different opening diameters under W=200

and lengths. The particle count data were compiled over varying times, and the velocity profiles were derived from these observations. As the shoe's aperture widens, particle velocity at the pipe's terminus exhibits a discernible downward trend, maintaining a stable suspended flow condition with minimal temporal fluctuations. At β=30°, particle accumulation over time reveals a steady increment for the five opening diameters. Notably, the quantities for openings of N=150 mm and 200 mm are aligned, displaying a higher volume than the three other openings.

This observation underscores the fragile balance between optimal aperture size and particle flow dynamics. Excessively large or small openings disrupt the intended flow pattern.

At β=45°, the particle count for apertures of N=100, 150, and 200 mm demonstrated a consistent rise over time. By contrast, particle number at N=250 mm experienced significant fluctuations, while the count at N=300 mm increased abruptly within a short time frame, a phenomenon that impedes efficient particle transport. When β=60°, the particle numbers for N=100 mm and N=300 mm initially increased before stabilizing. The diameter opening of N=100 mm led to particle accumulation within the shoe, while the excessively large aperture of N=300 mm resulted in particles migrating back to the left side of the shoe, yielding a lower particle count. For openings of N=150, 200, and 250 mm, particle number exhibited periodic fluctuations of varying amplitudes, which was indicative of the formation of material plugs within the pipeline. Notably, the amplitude of these fluctuations diminished with increasing opening size, correlating with a reduction in the magnitude of the material plugs.

The aperture dimensions significantly influence the internal pressure of the feeding shoe, because the pressure difference between the inlet and the outlet of the particle undergoes substantial alterations, ultimately affecting conveying performance. Consequently, an examination of pressure variations at each opening diameter across varying inclinations is conducted, with focus on relative pressure. In accordance with the analysis in Fig. 17, pipe pressure exhibits a gradual decline from the inlet to the outlet. The inlet region, which is characterized by the confluence of materials and gas, emerges as a high-pressure zone, a consequence of the resistance imparted by descending particles against gas flow. Consequently,

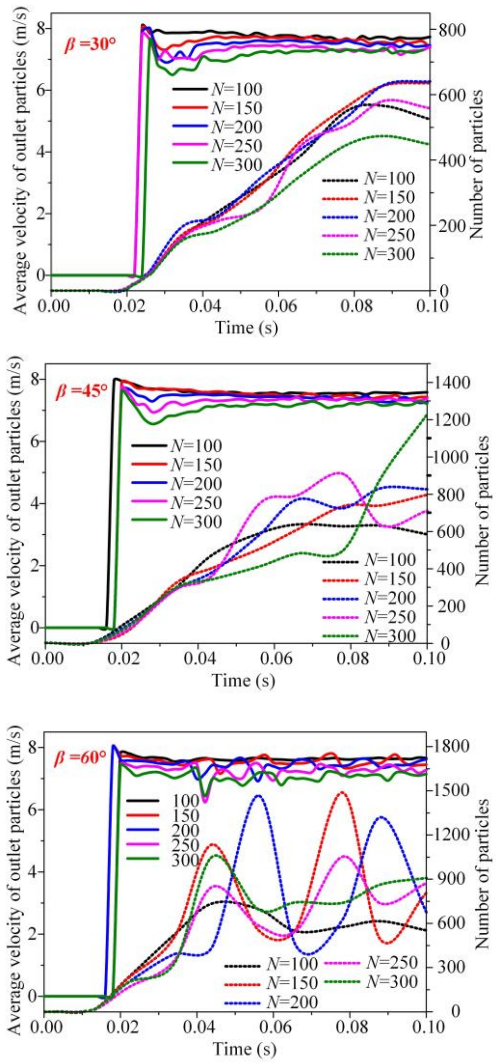

Fig. 16 Velocity and quantity of the outlet particles

the flux within the pipe diminishes, and pressure concurrently increases. By contrast, the outlet manifests as a low-pressure zone, with the maximum pressure exhibited within the pipe presenting a decreasing trend as opening diameter is incrementally augmented. When β=60° and the opening diameter is N=100 mm, the direction of the tube wall on the left side of the shoe is vertical, and no gas swirling is formed. When β=30° and the opening diameter is N=100 mm and 150 mm, pressure is lower than the other angles, an excessively shallow inclination angle promotes particle accumulation along the material shoe's right-side wall, significantly reducing particle throughput into the conveying pipeline. Simultaneously, an excessive opening diameter increases the left space of the material shoe, resulting in the upward reflux of particles, further reducing the particles that are entering the pipeline and reducing gas obstruction. The force on the gas from the inlet to the outlet decreases, gas flux increases, and eventually, pressure decreases.

To elucidate the nuanced alterations in pressure engendered by variations in aperture size, we meticulously plotted the axial pressure profiles from the entrance to the exit under three distinct angles, as shown in Fig. 18.

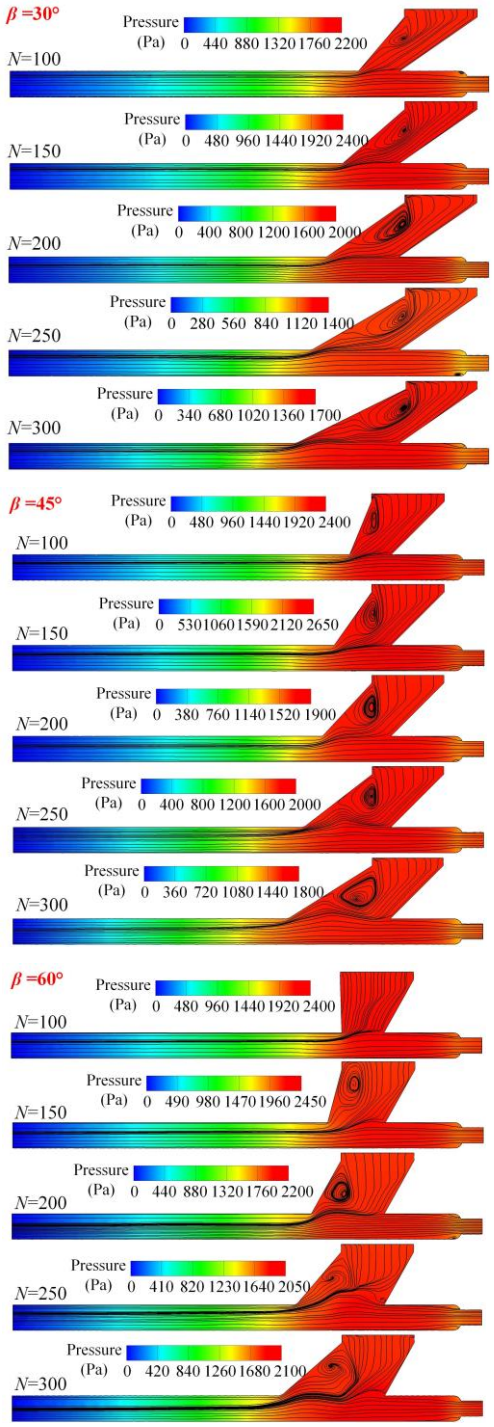

Fig. 17 Pressure drop in the tube with different opening diameters

Across these angles, axial pressure initially ascends, subsequently plateauing over a defined span, before ultimately declining. At β=30° and β=45°, inlet pressure across different apertures exhibit marked variability, with a discernible trend of progressive diminution as aperture size increases. Conversely, at β=60°, discrepancies in opening pressures are notably diminished, with axial pressure curves for N=100, 150, 200, and 300 mm are essentially overlapping. Furthermore, pressure differentials at the entrance for various apertures under β=60°, 45°, and 30° follow a gradient of decreasing magnitude.

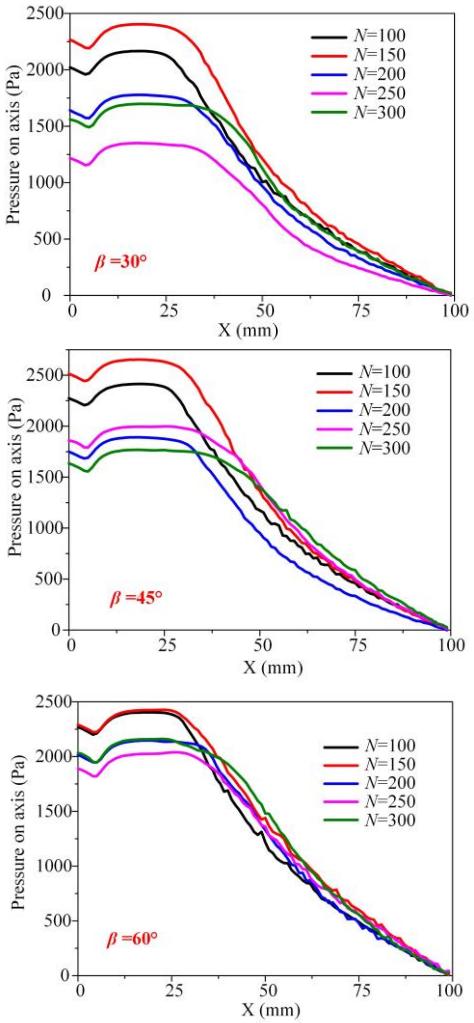

Fig. 18 Axial pressure of different opening diameters

4. CONCLUSIONS

The CFD–DEM method was used to analyze the gas–solid two-phase flow of a rotary valve's feeding shoes with different structures in a powder pneumatic conveying system, and the influence of feeding shoe structure on flow performance was studied. The key findings are summarized as follows:

(1) By comparing and analyzing the flow field characteristics of particles in the three structural forms of a rotary valve's feeding shoes (through, horn, and funnel types), the results indicate that the conveying capacity of funnel-type feeding shoe is poor. Moreover, the funnel-type shoe is more susceptible to particle accumulation and blockage at the feeding shoe position. Conversely, the through-type and horn-shaped feeding shoes demonstrate enhanced conveying efficacy and are less prone to blockage. However, a minor diameter of particle backflow is observed in the through and horn types.

(2) An investigation into the effect of varying the shoe inclination angle β on particle flow dynamics within the feeding shoe indicates that decreasing the inclination angle significantly diminishes particle flow. Consequently, particles tend to accumulate on the right wall of the shoe, hindering their entry into the conveying pipeline. This situation ultimately leads to blockage of the feeding port, compromising the overall efficiency of the pneumatic conveying system.

(3) In a comparative study on conveying efficacy within a shoe with varying opening configurations, we observed that under conditions of reduced opening size, conveyance efficacy bears a resemblance to that of a funnel-shaped configuration. However, particle escape velocity is significantly diminished, predisposing the system to blockages. Furthermore, when the lower opening of the shoe exceeds its upper opening, the leftward space within the shoe is prone to the development of swirling flow patterns. This condition results in gas-propelling particle backflow, which is detrimental to uninterrupted particle transport.

(4) It is found that the straight-through configuration system with "equal opening and large inclination angle" can significantly improve the particle conveying performance, reduce the probability of material blockage, and break through the engineering application stereotype of traditional funnel structure. This paper reveals the coupling mechanism between the variable diameter structure of the feed shoe and the dynamics of the gas-solid two-phase flow, breaking through the limitation that the traditional research focuses on the main pipeline and ignores the key transition structure. By establishing a two-parameter synergy model of opening-inclination, the quantitative influence of structural geometric characteristics on particle escape, reflux and blockage was clarified.

ACKNOWLEDGEMENTS

This study was supported by the Key R&D Program of Shandong Province, China (Grant No. 2024CXGC010403).

CONFLICT OF INTEREST

The authors declare that they have no known competing financial interests or personal relationships that could have appeared to influence the work reported in this paper.

AUTHORS CONTRIBUTION

Hongen Ge: Conceptualization, Formal analysis, Methodology, Validation, Writing–original draft, Writing –review & editing. **Juntao Li:** Data curation, Investigation, Visualization; **Liye Zhang:** Formal analysis, Writing – original draft; **Xin Zhang:** Supervision, Funding acquisition, Project administration, Resources; **Chunqi Zhao:** Software, Visualization, Writing –review & editing.

REFERENCES

Bu, F., Jiao, Y., & Wang, J. (2024). Novel close-clearance impeller structure for solid–liquid mixing at low reynolds numbers based on the paravisc impeller.

Industrial & Engineering Chemistry Research, *63*(35), 15585–15599. https://doi.org/10.1021/acs.iecr.4c02001

Chu, K., Chen, J., & Yu, A. (2016). Applicability of a coarse-grained CFD–DEM model on dense medium cyclone. *Minerals Engineering*, *90*, 43–54. https://doi.org/10.1016/j.mineng.2016.01.020

Dong, W., Zhang, X., Jiang, Z., Hu, X., Ge, Y., & Zhang, L. (2025). Study on structure design and parameter optimization of diversion rifled feeder based on CFD-DEM. *Agriculture-Basel*, *15*(3), 351. https://doi.org/10.3390/agriculture15030351

Gomes, T. L. C., Lourenço, G. A., Ataíde, C. H., & Duarte, C. R. (2021). Biomass feeding in a dilute pneumatic conveying system. *Powder Technology*, *391*, 321–333. https://doi.org/10.1016/j.powtec.2021.06.020

Gundogdu, M. Y. (2004). Design improvements on rotary valve particle feeders used for obtaining suspended airflows. *Powder Technology*, *139*(1), 76–80. https://doi.org/10.1016/j.powtec.2003.10.010

Guo, X., Lu, W., Lu, H., Cong, X., Xie, K., Liu, H., & Gong, X. (2013). Pressure drop prediction for horizontal dense-phase pneumatic conveying of pulverized coal associated with feeding to gasifier. *Chemical Engineering Research and Design*, *91*(12), 2509–2514. https://doi.org/10.1016/j.cherd.2013.04.012

Hou, P., Besenhard, M. O., Halbert, G., Naftaly, M., & Markl, D. (2023). Development and implementation of a pneumatic micro-feeder for poorly-flowing solid pharmaceutical materials. *International Journal of Pharmaceutics*, *635*, 122691. https://doi.org/10.1016/j.ijpharm.2023.122691

Lourenço, G. A., Gomes, T. L. C., Duarte, C. R., & Ataíde, C. H. (2019). Experimental study of efficiency in pneumatic conveying system's feeding rate. *Powder Technology*, *343*, 262–269. https://doi.org/10.1016/j.powtec.2018.11.002

Macchini, R., Bradley, M. S. A., & Deng, T. (2013). Influence of particle size, density, particle concentration on bend erosive wear in pneumatic conveyors. *Wear*, *303*(1–2), 21–29. https://doi.org/10.1016/j.wear.2013.02.014

Pezo, L., Banjac, V., Pezo, M., Jovanović, A. P., Đuragić, O., Čolović, D., & Čolović, R. (2021). Mathematical model, numerical simulation and optimization of rotating valve feeder in animal feed production. *Animal Feed Science and Technology*, *272*, 114741. https://doi.org/10.1016/j.anifeedsci.2020.114741

Saleh, K., Traore Ndama, A., & Guigon, P. (2011). Relevant parameters involved in tribocharging of powders during dilute phase pneumatic transport. *Chemical Engineering Research and Design*, *89*(12), 2582–2597. https://doi.org/10.1016/j.cherd.2011.06.001

Saluja, G., Mallick, S. S., & Karmakar, S. (2024). Predicting pneumatic conveyability and flowability of fly ash using bulk property characterization. *Particulate Science and Technology*, *42*(3), 482–494. https://doi.org/10.1080/02726351.2023.2261420

Santo, N., Portnikov, D., Eshel, I., Taranto, R., & Kalman, H. (2018a). Experimental study on particle steady state velocity distribution in horizontal dilute phase pneumatic conveying. *Chemical Engineering Science*, *187*, 354–366. https://doi.org/10.1016/j.ces.2018.04.058

Santo, N., Portnikov, D., Tripathi, N. M., & Kalman, H. (2018b). Experimental study on the particle velocity development profile and acceleration length in horizontal dilute phase pneumatic conveying systems. *Powder Technology*, *339*, 368–376. https://doi.org/10.1016/j.powtec.2018.07.074

Schadauer, C., Martetschläger, G. R., Ilie, A. L., Angerbauer, A., & Lanzerstorfer, C. (2020). Casting powders: Influence of the humidity on the flowability. *Ironmaking & Steelmaking*, *47*(5), 460–463. https://doi.org/10.1080/03019233.2020.1725730

Shang, K., Li, Y., Song, H., Xu, X., & Zhang, H. (2024). Research on flow field characteristics of curved pipe in bulk grain cyclone conveying based on gas solid coupling. *Journal Of Food Process Engineering*, *47*(9), e14725. https://doi.org/10.1111/jfpe.14725

Shang, K., Li, Y., Xu, X., Zhang, Y., & Zhang, Y. (2023). Study on the flow field characteristics of bulk grain pipeline based on gas-solid heterogeneous coupling. *Cogent Food & Agriculture*, *9*(1), 2219472. https://doi.org/10.1080/23311932.2023.2219472

Sharma, A., & Mallick, S. (2019). An investigation into pressure drop through bends in pneumatic conveying systems. *Particulate Science and Technology*, *39*, 1–12. https://doi.org/10.1080/02726351.2019.1676348

Sun, Z., Chen, L., Gao, K., Ma, G., Ma, H., Li, P., & Zhang, Y. (2023). Additional pressure loss coefficient of pneumatic conveying of moist-mixed materials for shotcrete based on CFD-DEM method. *Journal Of Building Engineering*, *76*, 107242. https://doi.org/10.1016/j.jobe.2023.107242

Versteeg, H. K., & Malalasekera, W. (1995). *An Introduction to Computational Fluid Dynamics*. An Introduction to Computational Fluid Dynamics. http://www.researchgate.net/publication/30875936

Wang, Z., Wang, T., Zhou, M., & Zhao, L. (2024). CFD modeling of gas–solid flow in a two-stage jetting fluidized bed with an overflow standpipe. *Asia-Pacific Journal of Chemical Engineering*, *20*(1). https://doi.org/10.1002/apj.3163

Woodruff, R. B., Kreider, P., & Weimer, A. W. (2012). A novel brush feeder for the pneumatic delivery of dispersed small particles at steady feed rates. *Powder Technology*, *229*, 45–50. https://doi.org/10.1016/j.powtec.2012.06.002

Wu, C., Zhao, L., & Cao, Z. (2024). Collision energy analysis within the vertical shaft impact crusher based

on the computational fluid dynamics-discrete element method. *ACS Omega*, acsomega.3c08017. https://doi.org/10.1021/acsomega.3c08017

Wypych, P. W., Hastie, D. B., Frew, I., & Cook, D. M. (2006). An experimental investigation into the feed rate capacity of rotary valve and blow tank feeders. *Particulate Science and Technology*, *24*(2), 165–179. https://doi.org/10.1080/02726350500544216

Yan, F., & Rinoshika, A. (2012). Characteristics of particle velocity and concentration in a horizontal self-excited gas–solid two-phase pipe flow of using soft fins. *International Journal of Multiphase Flow*, *41*, 68–76. https://doi.org/10.1016/j.ijmultiphaseflow.2012.01.004

Yao, J., Wang, C. H., Wee Chuan Lim, E., & Bridgwater, J. (2006). Granular attrition in a rotary valve: Attrition product size and shape. *Chemical Engineering Science*, *61*(11), 3435–3451. https://doi.org/10.1016/j.ces.2005.12.013

Zhang, F., O'Mahony, J. A., Miao, S., & Cronin, K. (2023). An Experimental Study on the Dilute Phase Pneumatic Conveying of Fat-Filled Milk Powders: Particle Breakage. *Powders*, *2*(1), 1. https://doi.org/10.3390/powders2010009

Zhang, X., Zhao, C., Ge, H., Liu, Z., Liu, Y., & Jiao, L. (2024). Analysis of gas-solid flow characteristics in intricate pipelines. *Chemical Engineering Research and Design*, *204*, 438–449. https://doi.org/10.1016/j.cherd.2024.03.010

Zhao, Y., Dahiphale, S., Tan, Y. Z., Wang, C. H., & Chew, J. W. (2020). The effect of particle initial charge on minimum pickup velocity (*U*pu) in pneumatic conveying. *Chemical Engineering Research and Design*, *156*, 343–352. https://doi.org/10.1016/j.cherd.2020.02.013

Zhou, F., Hu, S., Liu, Y., Liu, C., & Xia, T. (2014). CFD–DEM simulation of the pneumatic conveying of fine particles through a horizontal slit. *Particuology*, *16*, 196–205. https://doi.org/10.1016/j.partic.2014.03.015

Zhou, J., Ba, H., Yan, X., & Shangguan, L. (2023). Solid friction coefficient in a horizontal straight pipe of pneumatic conveying. *Chemical Engineering Research and Design*, *196*, 577–587. https://doi.org/10.1016/j.cherd.2023.07.001